JOURNAL OF GEOPHYSICAL RESEARCH, VOL. 112, B07317, doi:10.1029/2006JB004608, 2007

Global mantle flow and the development of seismic anisotropy: Differences between the oceanic and continental upper mantle

Clinton P. Conrad,[1] Mark D. Behn,[2] and Paul G. Silver[3]

Received 2 July 2006; revised 26 March 2007; accepted 10 April 2007; published 26 July 2007.

[1] Viscous shear in the asthenosphere accommodates relative motion between Earth's surface plates and underlying mantle, generating lattice-preferred orientation (LPO) in olivine aggregates and a seismically anisotropic fabric. Because this fabric develops with the evolving mantle flow field, observations of seismic anisotropy can constrain asthenospheric flow patterns if the contribution of fossil lithospheric anisotropy is small. We use global viscous mantle flow models to characterize the relationship between asthenospheric deformation and LPO and compare the predicted pattern of anisotropy to a global compilation of observed shear wave splitting measurements. For asthenosphere >500 km from plate boundaries, simple shear rotates the LPO toward the infinite strain axis (ISA, the LPO after infinite deformation) faster than the ISA changes along flow lines. Thus we expect the ISA to approximate LPO throughout most of the asthenosphere, greatly simplifying LPO predictions because strain integration along flow lines is unnecessary. Approximating LPO with the ISA and assuming A-type fabric (olivine *a* axis parallel to ISA), we find that mantle flow driven by both plate motions and mantle density heterogeneity successfully predicts oceanic anisotropy (average misfit 13°). Continental anisotropy is less well fit (average misfit 41°), but lateral variations in lithospheric thickness improve the fit in some continental areas. This suggests that asthenospheric anisotropy contributes to shear wave splitting for both continents and oceans but is overlain by a stronger layer of lithospheric anisotropy for continents. The contribution of the oceanic lithosphere is likely smaller because it is thinner, younger, and less deformed than its continental counterpart.

Citation: Conrad, C. P., M. D. Behn, and P. G. Silver (2007), Global mantle flow and the development of seismic anisotropy: Differences between the oceanic and continental upper mantle, *J. Geophys. Res.*, *112*, B07317, doi:10.1029/2006JB004608.

1. Introduction

[2] Convection in the Earth's mantle drives the tectonic motions of Earth's lithospheric plates as well as viscous deformation of the mantle rocks beneath them [e.g., *Turcotte and Oxburgh*, 1967]. Above a depth of ~300 km [e.g., *Hirth and Kohlstedt*, 2003], this deformation occurs as dislocation creep [*Karato and Wu*, 1993], which aligns olivine crystals into a lattice-preferred orientation (LPO) [*McKenzie*, 1979; *Ribe*, 1989]. Because olivine crystals are anisotropic [e.g., *Verma*, 1960], the development of LPO produces a macroscopic anisotropy in the uppermost upper mantle that can be detected seismically [e.g., *Hess*, 1964; *Forsyth*, 1975; *Montagner*, 1994]. This implies that observations of seismic anisotropy can in principle be used to constrain the sublithospheric mantle deformation that produces this anisotropy. However, the development of the LPO in upper mantle rocks is dependent on the finite strain history of olivine fabric [e.g., *Ribe*, 1992] as well as the effects of dynamic recrystallization, subgrain rotation, grain boundary migration [e.g., *Zhang and Karato*, 1995], and the presence of water [*Jung and Karato*, 2001] and melt [*Holtzman et al.*, 2003]. Because each of these effects introduce complexity into the prediction of LPO from a given mantle flow field [e.g., *Kaminski and Ribe*, 2001; *Blackman et al.*, 2002; *Kaminski et al.*, 2004], controversy continues over how observations of seismic anisotropy should be used to constrain geodynamic models of mantle flow [e.g., *Savage*, 1999; *Becker*, 2006a]. In this work, we resolve some of this controversy by comparing observations of upper mantle anisotropy with predictions made using global models of present-day mantle flow. In doing so, we identify regions where anisotropy is controlled by viscous mantle flow and estimate the importance of finite strain history on LPO development.

[3] Despite the uncertainty over the relationship between mantle flow and LPO, several studies have used observations of seismic anisotropy to constrain geodynamic models. In the simplest case the direction of observed anisotropy is taken as a direct indicator of mantle flow. This approach

[1]Department of Earth and Planetary Sciences, Johns Hopkins University, Baltimore, Maryland, USA.
[2]Department of Geology and Geophysics, Woods Hole Oceanographic Institution, Woods Hole, Massachusetts, USA.
[3]Department of Terrestrial Magnetism, Carnegie Institution of Washington, Washington, D. C., USA.

0148-0227/07/2006JB004608$09.00

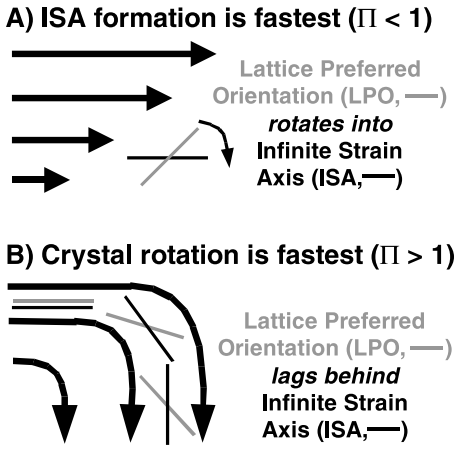

Figure 1. Comparison of (a) simple shear flow, in which the lattice-preferred orientation (LPO, gray line) rotates toward the infinite strain axis (ISA, black line) as it is exposed to finite strain, with (b) a more complicated flow in which crystal rotation by the flow occurs faster than ISA development. This causes the LPO to lag behind the ISA.

implicitly assumes A-type olivine fabric, in which the seismically fast a axis orients subparallel to the direction of maximum shear [*Jung and Karato*, 2001]. Basic patterns of flow around slabs [e.g., *Russo and Silver*, 1994; *Peyton et al.*, 2001], hot spots [e.g., *Walker et al.*, 2005; *Xue and Allen*, 2005], and ridges [e.g., *Wolfe and Solomon*, 1998] have been deduced in this manner. An alternative approach is to use seismic anisotropy to evaluate global models of mantle flow driven by plate motions and (tomographically inferred) mantle density heterogeneity. Despite employing different degrees of complexity in the prediction of LPO from flow, these studies tend to successfully predict the direction of anisotropy in oceanic regions. For example, several studies have simply used the horizontal projection of the instantaneous (strain rate) maximum shear direction to predict anisotropy determined from SKS shear wave splitting measurements [*Behn et al.*, 2004; *Hammond et al.*, 2005] and surface wave anisotropy [*Gaboret et al.*, 2003]. More sophisticated treatments for predicting LPO include finite strain accumulation [*Becker et al.*, 2003] and full fabric development models that incorporate the effects of dynamic recrystallization and subgrain rotation [*Becker et al.*, 2006a, 2006b]. However, despite differences in how LPO is inferred from the flow field, all of these global studies do an excellent job of predicting anisotropy in oceanic regions. In the analysis below, we show why these studies make similar predictions for LPO and in doing so introduce some simplicity into the discussion over how to predict LPO from models of mantle flow.

[4] Upper mantle anisotropy has been attributed to both asthenospheric and lithospheric sources. We expect anisotropy to be actively forming in the asthenosphere (the 100–200 km thick low-viscosity region beneath the lithosphere) where the relative motion between the surface plates and the upper mantle is accommodated [e.g., *Park and Levin*, 2002]. In contrast, mantle lithosphere is not experiencing active deformation because of its strength. Thus present-day plate motions probably do not induce lithospheric anisotropy, except in areas of active rifting or orogeny [e.g., *Silver*, 1996]. On the other hand, the lithosphere may preserve anisotropic fabric associated with past deformation [e.g., *Savage*, 1999; *Silver et al.*, 2001, 2004, 2006]. Thus, while recent mantle flow likely controls asthenospheric anisotropy, lithospheric anisotropy may contain fossil anisotropic fabric unrelated to flow in the present-day mantle. This fossil fabric can limit the usefulness of observed anisotropy for constraining present-day mantle flow patterns. However, if the influence of lithospheric anisotropy can be removed (e.g., by inverting shear wave splitting data for a two-layer model [*Silver and Savage*, 1994] or by utilizing the depth dependence of surface waves) the remaining asthenospheric anisotropy can place useful constraints on present-day mantle flow. First, however, the relative importance of lithospheric and asthenospheric anisotropy must be characterized for different tectonic regions [e.g., *Assumpcão et al.*, 2006; *Fouch and Rondenay*, 2006].

[5] The most obvious tectonic variation on the Earth's surface is the one between oceanic and continental lithosphere. Continental lithosphere is typically older, thicker, and has a longer deformation history than oceanic lithosphere. For this reason, *Silver* [1996] hypothesized that preserved fossil anisotropy, unrelated to present-day mantle flow, is more prevalent in continental lithosphere than in oceanic lithosphere. It is also likely that the upper mantle viscosity structure is simpler beneath the oceans. Although the thickness of oceanic lithosphere increases with age, it reaches a fairly uniform thickness of ~100 km for ages greater than ~50 Ma [e.g., *Stein and Stein*, 1992]. By contrast, continental lithosphere features "roots" that penetrate up to ~400 km beneath cratonic shields [e.g., *Jordan*, 1975; *Ritsema et al.*, 2004]. These deeply penetrating roots are likely cold and highly viscous relative to the surrounding asthenosphere [*Rudnick et al.*, 1998] and may extend through the asthenosphere [*Gung et al.*, 2003]. Such large lateral variations in viscosity will significantly influence the asthenospheric flow field beneath continents [*Fouch et al.*, 2000]. On the other hand, it is likely that the viscosity structure beneath oceans more closely resembles the layered structures that have been employed by most mantle flow models to date [e.g., *Becker et al.*, 2003; *Gaboret et al.*, 2003; *Behn et al.*, 2004].

[6] Although lateral viscosity variations have been employed in studies that predict lithospheric stresses [*Conrad and Lithgow-Bertelloni*, 2006], the geoid and dynamic topography [*Zhang and Christensen*, 1993; *Çadek and Fleitout*, 2003], net lithosphere rotation [*Zhong*, 2001; *Becker*, 2006], and plate motions [*Wen and Anderson*, 1997; *Becker*, 2006], only recently have lateral viscosity variations been included in flow models that predict seismic anisotropy [*Becker et al.*, 2006a]. In this study, we investigate the influence of laterally varying upper mantle viscosity in an effort to characterize the relative importance of asthenospheric and lithospheric anisotropy in both continental and oceanic regions.

2. Development of Seismic Anisotropy in the Asthenosphere

[7] To study the development of LPO in the sublithospheric mantle, we first consider the case of simple shear flow (Figure 1a). This flow pattern is expected throughout

most of the asthenosphere, as the differential motion between the lithosphere and the upper mantle is accommodated within the low-viscosity asthenosphere. In water-rich and/or high-stress environments, shear deformation may produce several different types of anisotropic fabric [*Jung and Karato*, 2001], some of which are not always parallel to the maximum shear direction [e.g., *Jung and Karato*, 2001; *Katayama et al.*, 2004]. Although these more unusual fabrics may be important in certain regions such as the fore-arc mantle wedge above slabs [e.g., *Kneller et al.*, 2005], the A-type fabric is expected to dominate for most regions of the asthenosphere [e.g., *Ismail and Mainprice*, 1998]. For A-type fabric, *Zhang and Karato* [1995] showed that for small strains the seismically fast olivine a axis will be oriented 45° to the direction of maximum shear (Figure 1a). However, for larger strains (>∼100%), the a axis will rotate into the maximum shear direction [*Zhang and Karato*, 1995]. Therefore, for asthenospheric simple shear (horizontal shear plane), the horizontal projection of LPO will be identical at both small and large strain and this approximation for LPO has been used by several authors [e.g., *Gaboret et al.*, 2003; *Behn et al.*, 2004] to predict observed anisotropy. It is important to remember that these studies implicitly assume that asthenospheric anisotropy forms quickly and does not depend on deformation history. However, shear flow in the asthenosphere may be more complex due to spatial variations in lithospheric thickness and time variations in asthenospheric flow patterns. In these cases, finite strain accumulation must be considered [e.g., *Becker et al.*, 2003, 2006a, 2006b].

[8] To determine the conditions under which it is necessary to integrate LPO along flow lines, *Kaminski and Ribe* [2002] introduced the infinite strain axis (ISA). The ISA is defined as the asymptotic orientation of the long axis of the finite strain ellipsoid after unlimited exposure to a given unchanging velocity gradient tensor. Thus the ISA can be defined for every point and time within a given time-variable flow field. However, if the rotational characteristics of the flow field are large compared to the straining characteristics, then the finite strain ellipsoid will rotate faster than it will develop; in this case the ISA does not exist [*Kaminski and Ribe*, 2002]. Because the olivine a axis aligns with the finite strain ellipsoid for A-type fabric [*Zhang and Karato*, 1995], the ISA should approximate LPO in the upper mantle if the velocity gradient tensor remains constant for olivine crystals moving along flow lines. However, if the velocity gradient tensor does not remain constant (as will generally be the case), then the ISA direction itself may change with time. The ISA will only be a good approximation for LPO if olivine crystals rotate toward the ISA more rapidly than the ISA changes along flow lines [*Kaminski and Ribe*, 2002].

[9] *Kaminski and Ribe* [2002] showed that the timescale for ISA development, τ_{ISA}, depends on the flow field but can be approximated by $\tau_{ISA} \sim \dot{\varepsilon}^{-1}$ where $\dot{\varepsilon}$ is the absolute value of the largest eigenvalue of the strain rate tensor. Thus the rate at which the LPO rotates toward the ISA can be estimated as $\Omega_{ISA} \sim \dot{\varepsilon}$. For simple shear (Figure 1a), the ISA is parallel to the direction of flow (i.e., the direction of maximum shear). Thus studies that use anisotropy observations to infer a flow direction [e.g., *Russo and Silver*, 1994; *Wolfe and Solomon*, 1998; *Peyton et al.*, 2001; *Walker et al.*, 2005; *Silver and Holt*, 2002; *Xue and Allen*, 2005] implicitly assume simple shear. Note that the horizontal components of the initial LPO and the final ISA are parallel under simple shear because finite strain affects only the orientation of LPO in the vertical plane (Figure 1a).

[10] An olivine aggregate being advected through the mantle may experience temporal changes in the orientation of the ISA if the velocity gradient tensor varies spatially along flow lines or if the flow field changes with time. Spatial variations in the ISA will be present if, for example, mantle density heterogeneity imparts a vertical component to asthenospheric flow (Figure 1b), as we would expect above an upwelling or downwelling mantle. The ISA may vary with time at any given location if either surface plate motions or the mantle density heterogeneity field evolve with time. *Kaminski and Ribe* [2002] defined the rate of ISA rotation along flow lines, which we denote here as Ω_{flow} (the reciprocal of *Kaminski and Ribe*'s [2002] timescale τ_{flow}) as the rate of change of the angle, Θ, between the local flow direction and the local ISA. If the local ISA direction changes more rapidly along flow lines than the finite strain ellipsoid rotates toward the ISA, then the net LPO will depend on the strain history in a complex way. However, if the rate of ISA formation (Ω_{ISA}) is faster than the rate of ISA rotation (Ω_{flow}), then the past strain history is irrelevant, and the LPO approaches the ISA. To determine which rate is faster, *Kaminski and Ribe* [2002] introduced the "grain orientation lag" parameter:

$$\Pi = \Omega_{\mathrm{flow}}/\Omega_{\mathrm{ISA}} \tag{1}$$

They find that if $\Pi < 0.5$, the ISA is a good approximation for LPO, which greatly simplifies predictions of anisotropy from a given flow field as finite strain calculations are unnecessary.

3. Models for Global Asthenospheric Flow

[11] Although *Kaminski and Ribe* [2002] calculated Π for several idealized flow geometries, to date no studies have evaluated Π globally throughout the upper mantle. Here we construct a series of global mantle flow models, driven by combinations of mantle density heterogeneity and surface plate motions, to predict LPO within the asthenosphere. We use the ISA as an approximation for LPO, and then test the validity of this approximation by determining if $\Pi < 0.5$.

3.1. Flow Field Calculations

[12] We develop global mantle flow models using the spherical finite element code CitComS. CitComS has been benchmarked extensively and can handle more than 4 orders of magnitude variation in viscosity [*Moresi et al.*, 1996; *Zhong et al.*, 2000], including the lateral variations important for this study [e.g., *Zhong*, 2001]. We employ a free slip condition at the core-mantle boundary, but our choice of surface boundary conditions depends on how mantle flow is driven (described below). We use both layered and laterally varying viscosity structures for the lithosphere and asthenosphere (described below), which allows us to probe the influence of variable lithospheric thickness on asthenospheric flow and LPO development.

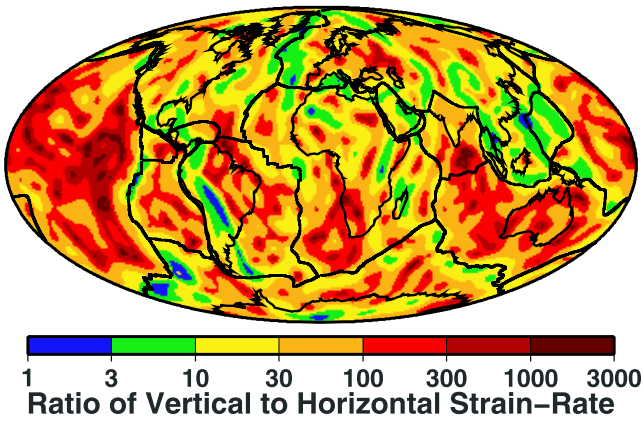

Figure 2. Ratio of the magnitude of vertical strain rates $\left(\dot{\varepsilon}_{\theta r}^2 + \dot{\varepsilon}_{\psi r}^2 + \dot{\varepsilon}_{rr}^2\right)^{1/2}$ to the magnitude of horizontal strain rates $\left(\dot{\varepsilon}_{\theta\theta}^2 + \dot{\varepsilon}_{\theta\psi}^2 + \dot{\varepsilon}_{\psi\psi}^2\right)^{1/2}$, averaged throughout the layered asthenosphere (100–300 km). Strain rates are shown that are calculated using the semianalytical spectral model of *Behn et al.* [2004], amended so that they can be compared to the finite element models presented here (i.e., we employ the S20RTSb tomography model and $\beta = 0.5$). For most locations, vertical gradients in velocity dominate the strain rate tensor.

3.1.1. Finite Element Grid

[13] We employ a global finite element grid with 874800 elements, including 24300 surface elements corresponding to 157 km horizontal resolution at the surface. Vertical resolution is 150 km in the lower mantle, 50 km in the upper mantle, and 25 km above 350 km. We chose to enhance the near-surface vertical resolution at the expense of horizontal resolution in order to better resolve the vertical gradients in velocity, which dominate LPO formation in the asthenosphere. As a result, we can accurately measure vertical gradients in both horizontal ($\partial v_\theta/\partial r$, $\partial v_\psi/\partial r$) and vertical ($\partial v_r/\partial r$) velocity ($\theta$, ψ, and r are the spherical coordinates), but measurement of horizontal gradients in velocity ($\partial v_\theta/\partial\theta$, $\partial v_\psi/\partial\theta$, $\partial v_r/\partial\theta$, $\partial v_\theta/\partial\psi$, $\partial v_\psi/\partial\psi$, $\partial v_r/\partial\psi$) is less accurate. This is not a problem for our calculation because the vertical length scale of the asthenosphere (~200 km) is much shorter than its horizontal length scale (typically thousands of kilometers). This causes the asthenospheric strain rate field to be dominated by its vertical components, which typically have magnitudes 10–1000 times greater than the horizontal components (Figure 2). Exceptions occur near plate boundaries (Nazca-Pacific) and immediately above upwelling (Africa) or downwelling (South America) flow. In these areas, vertical strain rates are still larger than horizontal strain rates, but by less than an order of magnitude (Figure 2). Because our enhanced vertical resolution allows us to resolve these gradients to comparable degrees, we can use our finite element grid to reproduce the flow fields produced by *Behn et al.* [2004], who used a semianalytical spectral method to calculate mantle flow [e.g., *Hager and O'Connell*, 1981].

3.1.2. Plate-Driven and Density-Driven Flow

[14] Following *Behn et al.* [2004], we drive instantaneous Stokes flow in the mantle using both mantle density heterogeneity inferred from seismic tomography (density-driven flow) and by imposing surface plate motions (plate-driven flow). For plate-driven flow, we impose NUVEL-1A plate motions [*DeMets et al.*, 1994] for 13 plates in the no-net rotation reference frame as velocity boundary conditions on the surface of the finite element grid. For density-driven flow, we employ rigid surface boundary conditions and assign densities in the mantle by converting velocity anomalies in the S20RTSb seismic tomography model [*Ritsema et al.*, 2004] to densities using a constant velocity-density conversion factor of 0.15 g cm^{-3} km^{-1} s. We chose this conversion factor because it is consistent with both laboratory data [e.g., *Karato and Karki*, 2001] and with previous studies [e.g., *Behn et al.*, 2004]. Also following previous work [e.g., *Lithgow-Bertelloni and Silver*, 1998; *Behn et al.*, 2004], we do not impose density anomalies above 325 km because seismically fast velocity anomalies associated with continental roots have been shown to correspond to neutrally buoyant "tectosphere" [e.g., *Jordan*, 1975]. This implies that a straightforward conversion between seismic velocity and density is not appropriate for the continental lithosphere. The 325 km depth approximates the maximum thickness of the African craton (Figure 3a), although *Behn et al.* [2004] showed that

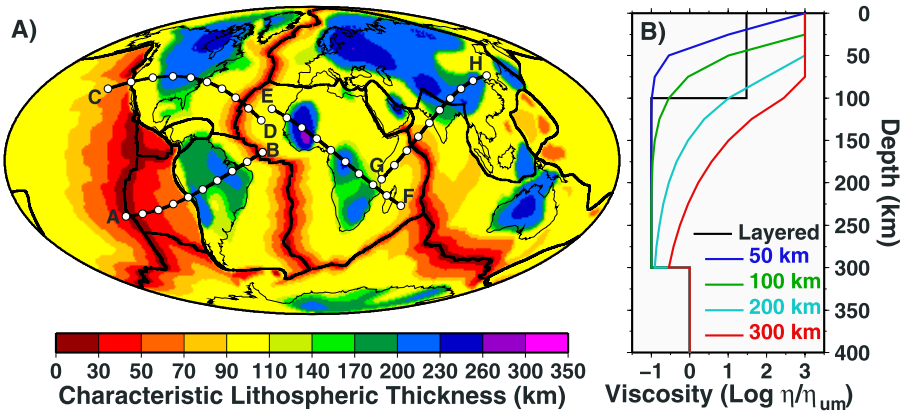

Figure 3. (a) Map of assigned characteristic lithospheric thickness and (b) the depth dependence of viscosity through the lithosphere and asthenosphere for the layered viscosity structure (black line) and for the laterally varying viscosity structure for different assigned characteristic lithospheric thicknesses (colored lines). Tracks in Figure 3a show the great circle paths of cross sections shown in Figures 4 and 5.

the choice of cutoff depth does not significantly affect the prediction of anisotropy at most stations.

[15] The actual flow field will be a combination of plate-driven and density-driven flow. Although it would be preferable to drive plate motions dynamically from density-driven flow, this is impractical for this study. Because asthenospheric shear flow is extremely sensitive to plate motion directions, it is important that our models include the proper plate motions to correctly compare predictions of anisotropy to observations. To combine density-driven and plate-driven flows, we followed the method of *Behn et al.* [2004], who noted that when plate motions are imposed, asthenospheric strain rates are set by the imposed plate velocities. By contrast, stresses are imposed for density-driven flow, making strain rates proportional to the magnitude of mantle viscosity. Thus the combined flow field depends on the absolute mantle viscosity assumed for the model. *Behn et al.* [2004] define a viscosity scale factor β by which to multiply the reference viscosity structure. This reference structure consisted of lower mantle (below 670 km), asthenospheric (100–300 km) and lithospheric (0–100 km) layers that were 50, 0.1, and 30 times as viscous as the upper mantle (300–670 km), which had a viscosity of 10^{21} Pa s prior to scaling by β. By varying β, *Behn et al.* [2004] solved for the viscosity structure that best fit 13 SKS shear wave splitting measurements from oceanic island stations in the Atlantic and Indian oceans. They found a best fit value of $\beta = 0.35$, corresponding to an upper mantle viscosity of 3.5×10^{20} Pa s. This value is consistent with the range in upper mantle viscosity (3 to 6×10^{20} Pa s) constrained from observations of postglacial rebound [*Mitrovica*, 1996]. In section 4.2 we employ a similar method to constrain the upper mantle viscosity structure, and find a similar best fitting value of $\beta = 0.5$ (implying an upper mantle viscosity of 5×10^{20} Pa s).

3.1.3. Layered Viscosity Versus Laterally Varying Viscosity

[16] To investigate the influence of lateral variations in viscosity associated with cooling oceanic lithosphere and deeply penetrating continental roots, we compare predictions of anisotropy made using a layered (spherically symmetric) viscosity structure with those made using a viscosity structure that includes lateral variations in viscosity. We employ the same layered viscosity profile used by *Behn et al.* [2004]. Following *Conrad and Lithgow-Bertelloni* [2006], we introduce lateral viscosity variations within the lithospheric and asthenospheric layers (without changing the viscosities of the upper and lower mantle layers) and assign a characteristic length scale for lithospheric thickness at every surface point on a finite element grid (Figure 3a). This "characteristic thickness" is used to define the depth dependence of viscosity through the lithosphere (Figure 3b). Oceanic lithosphere is assigned a thickness proportional to the square root of its age (taken from *Müller et al.* [1997]) and assuming a 100 km maximum thickness (Figure 3a). In continental areas, the characteristic thickness is determined from the maximum depth for which the velocity anomaly (from S20RTSb) is consistently greater than +2% [*Gung et al.*, 2003]. We imposed 100 km as the minimum continental thickness (Figure 3a). To introduce a smoothly varying viscosity structure, we impose an error function temperature profile above 325 km (below this depth we assign temperatures using the tomographic model) and use the characteristic lithosphere thickness for the length scale in the error function [*Conrad and Gurnis*, 2003]. By invoking temperature-dependent viscosity [*Hirth and Kohlstedt*, 1996] for this boundary layer, we create a region of stiff lithosphere that scales with the characteristic thickness and is underlain by a low-viscosity asthenosphere down to 300 km (Figure 3b). To achieve these profiles, we assume a pre-exponential term that produces an asthenosphere 10 times less viscous than the upper mantle (for direct comparison with the layered case), an activation energy of 200 kJ mol^{-1} for the temperature dependence, and a maximum viscosity 1000 times that of the upper mantle [see *Conrad and Gurnis*, 2003]. Although there exists significant uncertainty over the depth variation of viscosity near the surface, these parameters produce a relatively smooth transition from high-viscosity lithosphere to low-viscosity asthenosphere (Figure 3b). Note that at depths equivalent to the "characteristic thickness," the viscosity is smaller than that of the upper mantle (Figure 3b). Thus the lithosphere's effective (mechanical) thickness is typically smaller than the characteristic thickness defined here.

[17] We vary the asthenospheric viscosity by modifying the preexponential viscosity magnitude to produce a range of asthenospheric viscosities that are 0.03 (low-viscosity), 0.1 ("reference"), and 1.0 (no asthenosphere) times those of the upper mantle [see *Conrad and Lithgow-Bertelloni*, 2006]. We adjust the activation energy (using values of 300, 200, and 100 kJ mol^{-1}, respectively) so that lithospheric viscosities remain similar between these models despite changes in the preexponential factor.

3.2. Predictions of the Lattice-Preferred Orientation (LPO)

[18] *Kaminski and Ribe* [2002] showed that the ISA is a good approximation for LPO if the Grain Orientation Lag parameter Π (defined in equation (1)) is less than 0.5. Thus, to characterize LPO, we calculate both ISA and Π for the flow fields described above following the method of *Kaminski and Ribe* [2002]. To determine ISA requires knowledge of the velocity gradient tensor $L_{ij} = \partial v_i/\partial x_j$, which is difficult to measure accurately from the flow field. In the asthenosphere, the horizontal strain rates are significantly smaller than the vertical strain rates (as in Figure 2), implying that the elements in the third column of L_{ij} are much larger than those in the other two. We use this fact to form L_{ij} from the vertical components of the strain rate tensor: $L_{ij} = 0$ except for $L_{\theta r} = 2\dot{\varepsilon}_{\theta r}$, $L_{\psi r} = 2\dot{\varepsilon}_{\psi r}$, and $L_{rr} = \dot{\varepsilon}_{rr}$ [e.g., *Malvern*, 1969, chapter 4]. This approximation treats flow in the asthenosphere as horizontal shear flow (depicted in Figure 1a and governed by the $L_{\theta r}$ and $L_{\psi r}$ terms) perturbed by any vertically oriented component of flow (as shown in Figure 1b and given by the L_{rr} term). Note that for this approximation, the velocity gradient tensor **L** contains no rigid body rotation. As such the vorticity number $\Gamma = \Omega/\dot{\varepsilon}$, where Ω is the magnitude of the rotation tensor and $\dot{\varepsilon}$ is the magnitude of the strain rate tensor [*Kaminski and Ribe*, 2002], is always less than or equal to 1. This is because $\Omega = (\dot{\varepsilon}_{\theta r}^2 + \dot{\varepsilon}_{\psi r}^2)^{1/2}$ is always smaller than or equal to the largest eigenvalue of the strain rate tensor, which we can determine analytically to be $\dot{\varepsilon} = \dot{\varepsilon}_{rr}/2 + (\dot{\varepsilon}_{rr}^2/4 + \dot{\varepsilon}_{\theta r}^2 + \dot{\varepsilon}_{\psi r}^2)^{1/2}$. For two dimensions, *Kaminski and*

Ribe [2002] showed that the ISA exists if $\Gamma \leq 1$. For three-dimensional flow, the existence of the ISA depends on the relative orientations of the vorticity vector and the principal strain rate direction, and we take $\Gamma \leq \sim 1$ (meaning order unity) as the criterion for ISA existence in our calculations. For the shear flow approximation, if the horizontal strain rates ($\dot{\varepsilon}_{\theta r}$ and $\dot{\varepsilon}_{\psi r}$) are much larger than the radial strain rate ($\dot{\varepsilon}_{rr}$), then the flow approximates simple shear with $\Gamma \rightarrow 1$. If the radial component dominates (e.g., over an upwelling or a downwelling), then pure shear dominates and $\Gamma \rightarrow 0$. Since $\Gamma \leq \sim 1$ for both extremes, we can infer that the ISA exists throughout most of the asthenosphere. Note that the validity of this argument diminishes for regions where our horizontal shear flow approximation breaks down due to large horizontal variations in the flow field, as would be found near subduction zones. By following the method described by *Kaminski and Ribe* [2002, Appendix A] (note that their equation (A3) should be $U = FF^T$ as defined by *Malvern* [1969]), we are able to calculate ISA for asthenospheric flow.

[19] We next evaluate whether the ISA orientations are a valid approximation for LPO by calculating Π throughout the mantle flow fields described above. This involves calculating Ω_{ISA} and Ω_{flow}. The former is defined as the eigenvalue of the strain rate tensor with the largest absolute value. *Kaminski and Ribe* [2002] define the latter as

$$\Omega_{\mathrm{flow}} = \mathrm{D}\Theta/\mathrm{D}t = \partial\Theta/\partial t + \mathbf{u} \cdot \nabla\Theta \qquad (2)$$

where Θ is the angle between the local flow direction ($\mathbf{u}$) and the ISA. The second term on the right hand side of (2) represents changes in Θ as grains are advected along flow lines, and can be determined from the velocity field and the ISA direction. The first term represents changes in Θ due to the time dependence of the flow field. For density-driven flow, we measure this quantity by differencing measurements of Θ across 10 time steps (corresponding to a time Δt of $\sim$5 Ma for most runs), and dividing by Δt. The resulting quantity is typically comparable in magnitude to the advective term. By contrast, plate motions are thought to be steady or only gradually changing, except during times of plate reorganization [e.g., *Engebretson et al.*, 1984], which is not thought to be occurring presently [e.g., *Sella et al.*, 2002]. Thus time-dependent changes in Θ for plate-driven flow are likely to be small, and we have not included them here. We sum the advective and (density-driven) time-dependent changes in Θ to calculate Ω_{flow} throughout the mantle and divide by Ω_{ISA} (see equation (1)) to estimate Π for the present-day mantle.

[20] To confirm that the model resolution in our finite element flow model is sufficient to accurately determine ISA and Π, we compare predictions of these quantities made using the finite element grid described in section 3.1.1 (horizontal and vertical resolutions of 157 km and 25 km above 350 km depth) with predictions made using a grid with both coarser resolution (auxiliary material Figures S1a and S1c, horizontal and vertical resolutions of 210 km and 33 km) and finer resolution (Figures S1b and S1d, horizontal and vertical resolutions of 105 km and 17 km).[1] This comparison shows similar spatial patterns for both ISA and Π, both in planform (Figures S1a and S1b) and in cross section (Figures S1c and S1d), across a factor of two variation in model resolution. To estimate the uncertainty in our predictions of Π and ISA, we compared the output of our intermediate resolution model (used throughout this paper) with the output of the coarser (Figures S2a and S2b) and finer (Figures S2c and S2d) resolution models. These comparisons confirm that Π and ISA are not strongly sensitive to model resolution. The spatial patterns of errors shown in the two different resolution comparisons are poorly correlated to each other, which means that there is no systematic change in the error as the resolution improves. The observed uncertainty is the result of small horizontal or vertical changes in ISA direction, as well as sensitivity of the ISA direction to the relative amplitudes of the major axes of the finite strain ellipsoid (since the ISA is defined as the direction of the longest axis, an ambiguity exists if two axes are nearly equal in length). Because Π depends on spatial gradients of the ISA, the uncertainty in Π is correlated to the uncertainty in ISA. We find that the median difference in the azimuth of ISA (Figures S2a and S2c) is less than 5° for points at which $\Pi < 0.5$ (indicating that ISA approximates LPO) and the median discrepancy in the estimate of Π (Figure S1d) is less than a factor of 2 (Figure S2b and S2d). Thus we infer that uncertainty of this magnitude is inherent to our estimates of Π and ISA.

3.3. Grain Orientation Lag Parameter (Π)

[21] To investigate the distribution of Π throughout the upper mantle, we examine a sample cross section AB (which runs from the East Pacific Rise to the Mid-Atlantic Ridge, see track in Figure 3a) for both plate-driven flow (Figures 4a and 4b) and density-driven flow (Figures 4c and 4d), and several different cross sections for these two flows combined (using $\beta = 0.5$, Figure 5). For each of these cross sections, and for the global planform at 225 km depth (Figure 5a), we find that Π is less than 0.5 (corresponding to a log value of -0.3 shown in the center of the white band in Figures 4 and 5) throughout most of the asthenosphere and upper mantle. In some locations, such as within a band extending $\sim$150 km below the high-viscosity lithosphere, Π is typically orders of magnitude smaller than 0.5. For density-driven flow, the region of smallest $\Pi < 0.5$ is located between 20% and 55% of the distance from the asthenospheric roof to its base (Figure 6a, gray triangles). This region of diminished Π occurs because any vertical component of density-driven flow must spread or converge laterally when it interacts with the rigid lithosphere. The high strain rates associated with the resulting shear flow lead to diminished Π in the upper asthenosphere. By contrast, plate-driven flow induces a shear flow that is more evenly distributed throughout the asthenosphere, leading to more uniform values of Π through the layer (Figure 6a, white circles). The variation of Π within the asthenosphere is not significantly dependent on asthenospheric viscosity (Figure 6b), although lack of a low-viscosity asthenosphere decreases the number of points for which $\Pi < 0.5$ (Figure 6b).

[22] Regions of the asthenosphere with $\Pi > 0.5$ are typically associated with upwelling flow caused by divergence near ridges (Figures 4a, 4b, and 5b at 5° and 85°,

[1] Auxiliary materials are available in the HTML. doi:10.1029/2006JB004608.

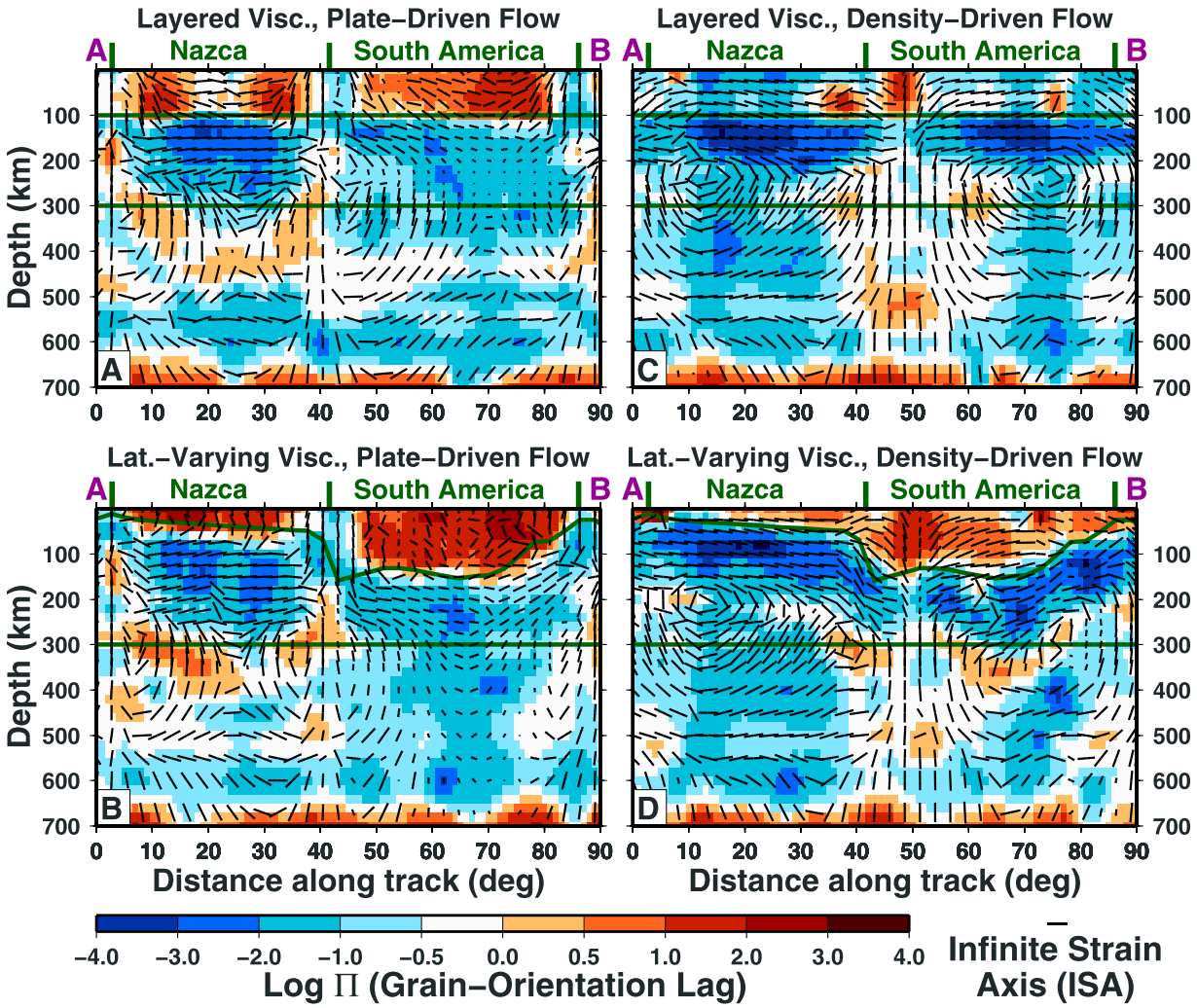

Figure 4. Cross sections showing Π (colors show base 10 log of Π) and the ISA (bars) through the upper mantle along cross section AB, which traverses the Nazca and South American plates (Figure 3a). Results (a and b) for flow driven by imposed plate motions and (c and d) for flow driven by mantle density heterogeneity. Both a layered viscosity structure (Figures 4a and 4c) and a laterally varying viscosity structure (Figures 4b and 4d) are imposed for the lithosphere and asthenosphere. The upper and lower boundaries of the low-viscosity asthenosphere, defined as the depths where viscosity crosses 10^{21} Pa s (Figure 3b), are highlighted by black lines. The vertical length axis is exaggerated by a factor of 9 so that vertical variations in Π and ISA can be viewed more easily. To maintain the ISA direction relative to the flow field, the vertical component of the ISA is exaggerated by the same factor. The magnitude of the ISA, however, is unity, so variations in the length of ISA bars represent changes in the component of ISA that is perpendicular to the cross section.

Figure 5c at 75°, Figure 5e at 25°) or downwelling flow associated with plate convergence (Figures 4a, 4b, and 5b at 40°). Downwelling flow caused by slab descent (the Nazca slab in Figures 4c, 4d, and 5b at 35°–65°, the Farallon slab in Figure 5c at 30°–50°, the Tethyan slab in Figure 5e at 60°–75°) or upwelling flow associated with slow seismic velocity anomaly (the African "superplume" in Figure 5d at 25°–75°) may also lead to Π > 0.5 in parts of the asthenosphere. However, away from plate boundaries, Π < 0.5 for the large majority of the asthenosphere (Figure 5a).

[23] The lower mantle (>660 km) shows large values of Π because its high viscosities result in small strain rates, leading to small values of Ω_{ISA}. By contrast, Ω_{flow} does not differ significantly between the upper and lower mantle, which indicates that the spatial and temporal gradients that characterize lower mantle flow are similar to those of the upper mantle. Because rates of ISA rotation in the lower mantle are similar to those in the upper mantle, the slower development of the ISA in the lower mantle (indicated by small Ω_{ISA}) may prevent the development of stable LPO there. This may explain the lack of a coherent anisotropic fabric in the lower mantle [e.g., *Meade et al.*, 1995], despite recent laboratory observations indicating that lower mantle perovskite deforms by dislocation creep [*Cordier et al.*, 2004]. Thus large Π in the lower mantle may be partly responsible for its isotropic nature.

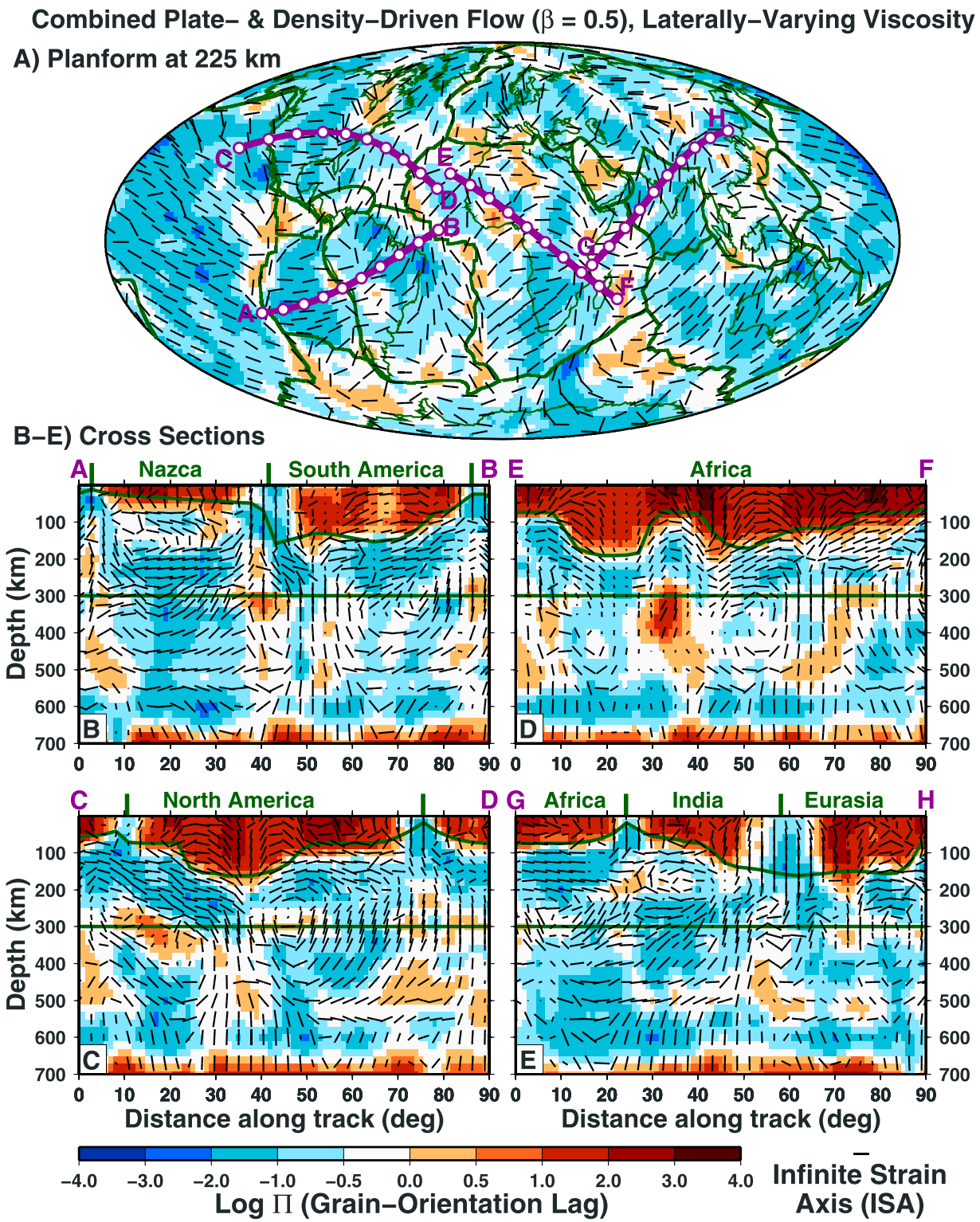

Figure 5. (a) Planform at the best fitting depth of 225 km and (b–d) cross sections showing Π (colors show base 10 log of Π) and ISA (bars) for a "preferred" flow model that combines plate-driven and density-driven flow (using $\beta = 0.5$), as described in the text. The surface paths (AB, CD, EF, and GH) of the cross sections (Figures 5b–5d) are shown in Figure 5a and in Figure 3a. The asthenosphere is bounded above and below by black lines as in Figure 4.

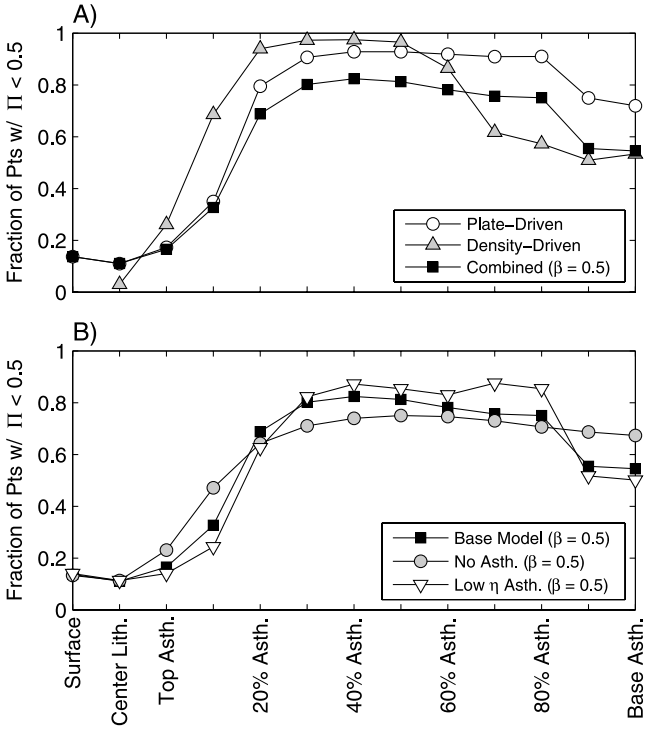

Figure 6. Fraction of points globally for which $\Pi < 0.5$, as a function of depth within the lithosphere and asthenosphere. Here depth is given as a fractional component of the thickness of each layer because the layer thicknesses vary laterally (Figure 3). The 0.5 cutoff is the value of Π below which the ISA approximates LPO given the effects of finite strain accumulation [*Kaminski and Ribe*, 2002]. (a) Tabulations for the case of laterally varying viscosity and plate-driven flow (white circles, Figure 4b), density-driven flow (gray triangles, Figure 4d), and the combination of the two flows (black squares, Figure 5). (b) Tabulations for combined plate-driven and density-driven flows ($\beta = 0.5$) assuming the asthenospheric viscosity of the base model of Figure 3 (black squares), or using asthenospheric viscosities that are 10 (which imparts no asthenospheric viscosity drop, gray circles) or 0.3 (low-viscosity case, white inverted triangles) times this value.

[24] Values of Π within the high-viscosity lithosphere are typically several orders of magnitude larger than 0.5 (Figures 4 and 5). In fact, most of the lithosphere can be distinguished from the asthenosphere by a large increase in Π. These large Π values result from slow anisotropic fabric development associated with small lithospheric strain rates. For these regions, prediction of anisotropic direction from a viscous flow model is difficult, if not impossible, because it requires an accurate integration of the strain history during the past 10–100 Myr. Therefore we ignore anisotropy predictions in the lithosphere where $\Pi > 0.5$. On the other hand, Π can be <0.5 for lithosphere near plate boundaries, where the discontinuity in plate motions leads to large strain rates (Figure 5). Although these large strain rates generate small values of Π, this study does not have the numerical resolution (157 km horizontal grid spacing) to resolve the detailed deformation occurring in these regions. More detailed studies of corner flow [*Kaminski and Ribe*, 2002] show that Ω_{flow} increases at plate boundaries, making $\Pi > 0.5$ likely in higher resolution studies. In fact, *Behn et al.* [2004] found that SKS observations at stations located <500 km from a mid-ocean ridge axis are best fit by the direction of spreading, which indicates that corner flow associated with local spreading dominates the observed anisotropy at near-ridge stations. Stations near subduction zones will also likely be similarly affected by local flow associated with the plate boundary, which would suggest increased Π. Similarly, convective instability, or other local flow disturbances with length scales comparable to our grid resolution, should increase Ω_{flow} and lead to larger values of Π than predicted here (Figure 5).

3.4. Infinite Strain Axis (ISA)

[25] Because $\Pi < 0.5$ throughout most of the asthenosphere, it is appropriate to use the ISA as an approximation for LPO within this layer. As discussed above, the ISA is most sensitive to shear deformation, and orients in the direction of maximum shear. For plate-driven flow, asthenospheric shear parallels plate motions, as does the ISA (Figures 4a and 4b, where flow is dominated by convergent Nazca and South American plate motions). For density-driven flow, horizontal shear accommodates motion between the stationary lithosphere and the flowing mantle. As discussed above, this shear occurs in the upper asthenosphere, where the ISA is parallel to the direction of uppermost mantle flow (e.g., Figures 4c and 4d, where flow is dominated by the downgoing Nazca slab at ~50°). For combined flows (Figure 5), the ISA direction generally dips parallel to the slope of the sublithospheric base and aligns in the direction of flow, except in a few regions near plate boundaries and upwellings where flow is nearly vertical.

[26] We evaluate the influence of lateral variations in lithospheric thickness on the ISA by comparing the layered and laterally varying viscosity structures (Figure 7). The predicted anisotropy direction changes significantly beneath thin lithosphere at some oceanic ridges, near some subduction zones, and on the edges of deeply penetrating conti-

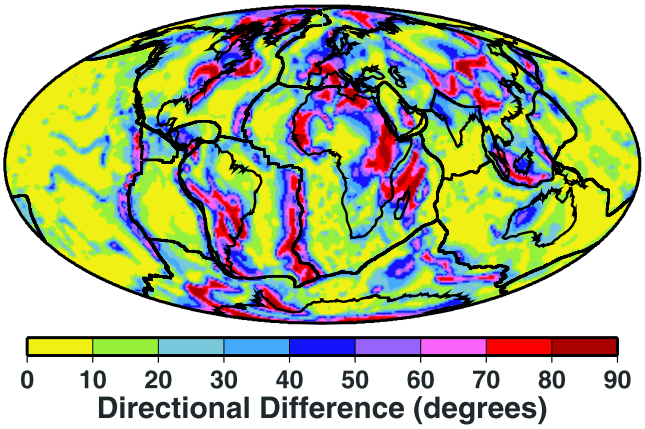

Figure 7. Comparison of the ISA direction at 225 km for laterally varying (Figure 5a) and layered viscosity structures. Plate-driven and density-driven flows are combined using $\beta = 0.5$.

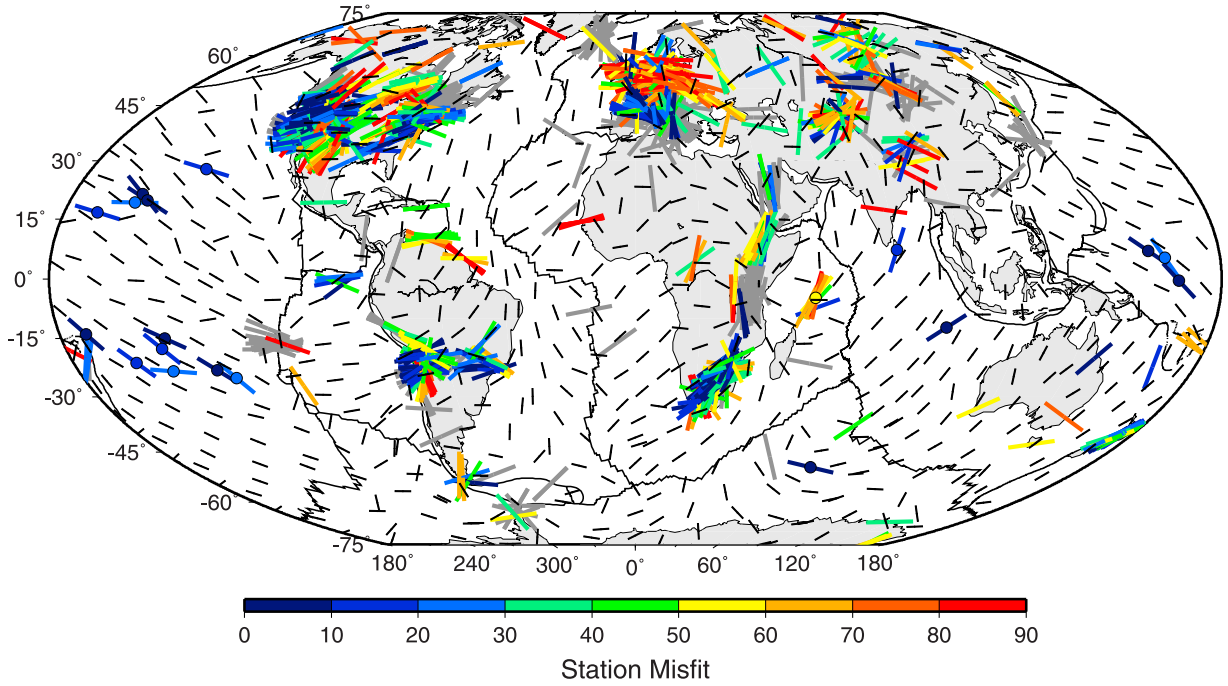

Figure 8. Comparison of the ISA direction for the "preferred" model (combined density-driven and plate-driven flows ($\beta = 0.5$) and lateral viscosity variations) at 225 km (black bars, as shown in Figure 5a) with the global compilation of SKS splitting directions. The directional misfit (in degrees) for each station is given by its color. Oceanic stations used in the global misfit calculation are shown with a central circle over the station location. Stations in gray are not used in the analysis because $\Pi > 0.5$ at 225 km, which indicates that our approximation of the ISA direction for the LPO may not be appropriate at these stations.

nental roots (e.g., eastern North America, Africa, Western Australia, Figure 7). These changes occur for two reasons. First, convergent or divergent flow at plate boundaries is sensitive to the viscosity structure because it includes a significant vertical component of flow. Second, increasing or decreasing the lithospheric thickness will increase or decrease the depth at which asthenospheric shear flow occurs. This may cause a given shear flow to move below or above the depth at which anisotropy is measured, thus changing the observed direction. On the other hand, only small changes in the ISA direction are observed beneath oceanic plates away from plate boundaries (Figure 7), where the laterally varying viscosity structure resembles the layered case (Figure 3b).

4. Comparison to Global SKS Splitting Data

[27] We compare the previously described predictions of asthenospheric anisotropy to a global data set of shear wave splitting measurements. In doing so, we seek to determine the absolute mantle viscosity structure (controlled by β) that yields the best fit to observed anisotropy. We also evaluate the importance of lateral viscosity variations and differences between the model fit to continental and oceanic anisotropy.

4.1. Global SKS Data Set

[28] The global shear wave splitting data set used in this study was derived from the Arizona State University Global Upper Mantle Anisotropy Data Set (http://geophysics.asu.edu/anisotropy/upper). This data set contains ~1350 splitting measurements (Figure 8) using SKS and SKKS phases compiled from 87 studies in oceanic and continental environments. In addition, we have supplemented this data set with several recent shear wave splitting studies in the ocean basins [*Wolfe and Silver*, 1998; *Smith et al.*, 2001; *Klosko et al.*, 2001; *Fontaine et al.*, 2005; *Hammond et al.*, 2005].

4.2. Inversion for the Best Fitting Flow Model

[29] Following the approach of *Behn et al.* [2004], we use the shear wave splitting data at 106 oceanic stations to constrain the viscosity scale factor β (see section 3.1.2). Initially, we exclude continental stations because continental lithosphere may preserve a fossil anisotropic fabric associated with past or ongoing lithosphere deformation [e.g., *Silver*, 1996]. Thus using continental stations to constrain β may result in the flow field being fit to lithospheric anisotropy unrelated to current mantle flow. We later test this assertion by performing a similar analysis for continental stations. Oceanic lithosphere is typically thinner and has a shorter, simpler, and less active deformation history than continental lithosphere. Thus lithospheric anisotropy in the oceans should be less significant for oceanic stations, and single layer anisotropy models (asthenosphere only) typically fit SKS splitting data at ocean island stations better than two layer models (asthenosphere and lithosphere) [*Behn et al.*, 2004].

[30] We exclude stations for which $\Pi > 0.5$ (at the comparison depth) because the ISA may not be a valid approximation for LPO in these locations. Furthermore,

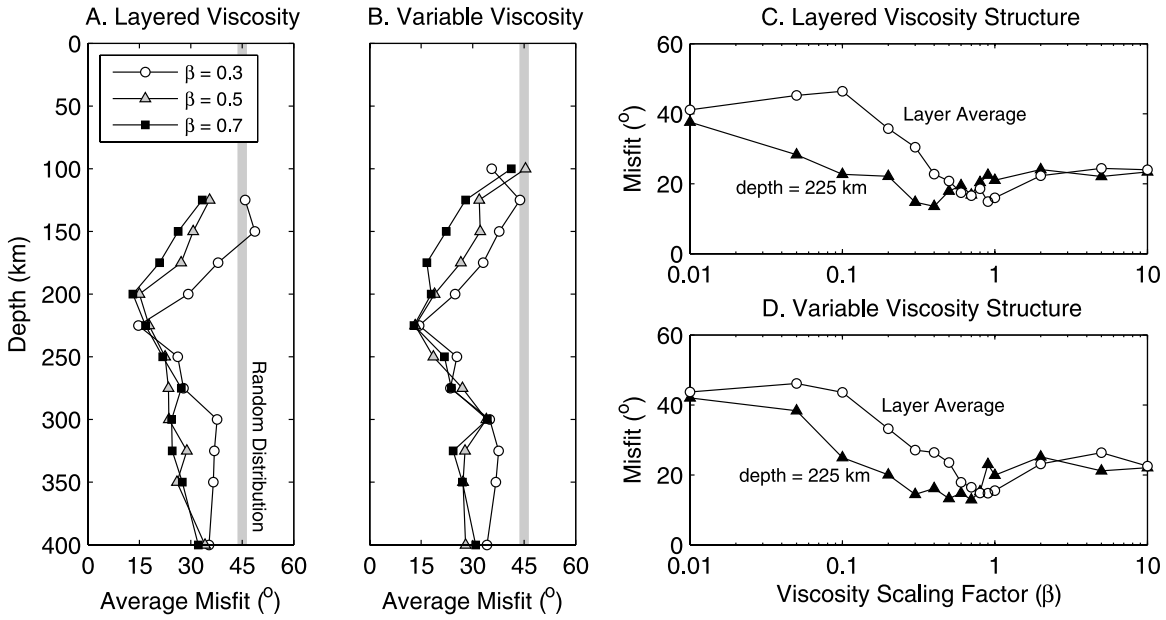

Figure 9. Average misfit for oceanic stations. (a) Layered viscosity and (b) laterally varying viscosity showing the variation of misfit with depth for different values of the viscosity scale factor β is shown (as defined by *Behn et al.* [2004]; see text). (c) A function of β for layered viscosity and (d) laterally varying viscosity showing the variation of misfit at 225 km (black triangles), which is the depth that provides the smallest misfit in Figures 9a and 9b, and the average misfit through the asthenospheric layer (white circles).

because we expect $\Pi > 0.5$ near plate boundaries (see section 3.3), we also exclude oceanic stations located <500 km from a plate boundary. For the inversions for β below, we are left with 19 "clean" oceanic stations (stations with circles in Figure 8) for which we know of no corrupting influences that would prevent us from comparing predicted anisotropy to observations. Only 8 of these 19 stations were used by *Behn et al.* [2004] to constrain β (five of their stations do not satisfy $\Pi < 0.5$).

[31] We first examine the variation of predicted anisotropy (ISA direction) as a function of depth within the asthenosphere, and compare it to the SKS splitting measurements made at these 19 oceanic stations. To do this, we measure the average misfit, which we define as the average angular difference between the predicted ISA direction and the SKS fast polarization direction, as a function of depth (Figures 9a and 9b). Since we exclude points for which $\Pi > 0.5$ this eliminates most points in the lithosphere (Figure 6). For values of β that bracket the $\beta = 0.35$ value obtained by *Behn et al.* [2004], we observe a region in the midasthenosphere (150–275 km depth) where both the layered (Figure 9a) and laterally varying (Figure 9b) models show a significantly improved fit to the oceanic SKS splitting observations compared to a random distribution (45°). For both cases, this region is centered around the same depth (~225 km) that *Behn et al.* [2004] used to compare the predicted and observed anisotropy directions. Examining the full range of β between density-driven flow only (small β) and plate-driven flow only (large β), we find a minimum in misfit for $\beta = 0.3–0.4$ at 225 km (Figure 9c) for layered viscosity and for $\beta = 0.3–0.7$ for laterally varying viscosity (Figure 9d). The average misfit for both layered and laterally varying viscosity cases is 13°, which is comparable to what *Behn et al.* [2004] found using a smaller SKS data set in the Atlantic and Indian oceans.

[32] SKS-related phases follow a nearly vertical path through the upper mantle, and thus represent a measure of the cumulative anisotropy in the asthenosphere. Thus it may be more appropriate to compare the splitting measurements to the average orientation of anisotropy throughout the asthenosphere, although for large variations with depth, the net anisotropy is a more complex function [*Rumpker and Silver*, 1998]. If we calculate the misfit for the average ISA direction for all asthenospheric depths where $\Pi < 0.5$, we find best fitting β values that range from 0.6 to 0.9 for both the layered viscosity (Figure 9c) and laterally varying (Figure 9d) viscosity structures. These β values are slightly larger than the preferred range for a single, best fitting depth, which implies larger asthenospheric viscosities and a greater role for plate-driven flow in determining anisotropy. As discussed above, plate-driven flow tends to produce a thicker region of coherent anisotropy than does density-driven flow (compare Figures 4a and 4b to Figures 4c and 4d, also note thickness of low Π values in Figure 6a). Thus larger values of β tend to produce a thicker layer of well fitting anisotropy (compare $\beta = 0.3$ to $\beta = 0.7$ curves in Figures 9a and 9b), and are preferred if we use the entire asthenospheric thickness to infer anisotropy. However, we obtain slightly better overall fits if we consider only the best fitting depth (Figure 9d), in which case a more concentrated layer of well fitting anisotropy is assumed.

[33] In general, values of β between 0.3 and 1.0 yield predictions of asthenospheric anisotropy that fit the oceanic SKS observations within the nominal uncertainty of the splitting observations [*Behn et al.*, 2004]. For this study, the model that gives the best overall fit to the oceanic compo-

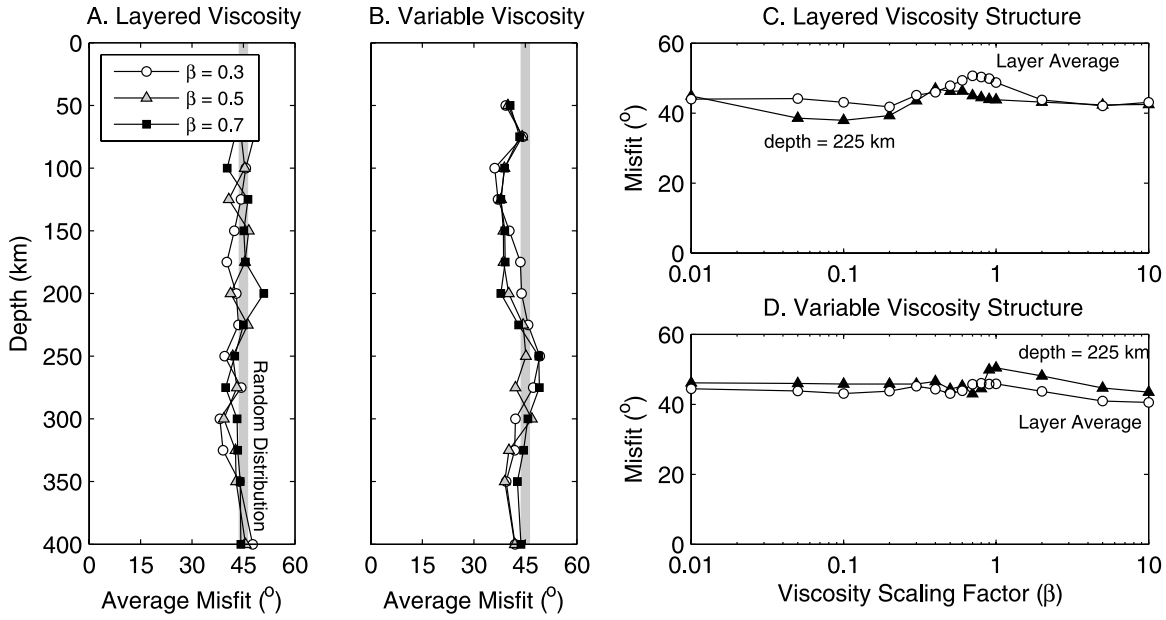

Figure 10. Average misfit for continental stations only, evaluated using the same method that was applied to oceanic stations (as in Figure 9). Compared to a random distribution (expected misfit of 45°), no value of the viscosity scale factor β significantly improves the continental misfit at 225 km (solid triangles, Figures 10c and 10d), the average misfit in the asthenosphere (open circles, Figures 10c and 10d), or the misfit at any particular layer within the asthenosphere (Figures 10a and 10b).

nent of our splitting data set is one that employs lateral viscosity variations and uses a value of $\beta = 0.5$ to define the relative importance of density-driven and plate-driven flows (Figure 9d). This successful prediction of sublithospheric anisotropy in the oceans validates the use of the ISA to predict LPO, the dominance of A-type fabric [*Jung and Karato*, 2001] in the asthenosphere, and the flow model itself.

4.3. Oceanic Versus Continental Anisotropy

[34] Our best fit model for suboceanic asthenospheric flow also predicts asthenospheric anisotropy beneath continental lithosphere. For continental stations with $\Pi < 0.5$ at 225 km, however, our preferred flow model produces an average fit to splitting measurements (Figure 8) that is significantly worse than it is for the oceanic stations, (41° for continents versus 13° for oceans for $\beta = 0.5$). However, since our choice of β is optimized to give the best fit to oceanic stations, we explore the possibility that a different value of β may provide an improved fit for continental areas (Figure 10). We find that at all depths, no value of β significantly improves the misfit compared to a random distribution (Figure 10). Thus it appears unlikely that a different value of β applies for continental regions, at least when averaged globally. This sharp contrast with the oceanic case (Figure 9) suggests differences between the anisotropic nature of the continental and oceanic upper mantles.

[35] A comparison of the distribution of misfit for oceanic and continental stations (assuming $\beta = 0.5$), also suggests major anisotropic differences. For oceanic stations, nearly 75% of stations are fit to within 20° at 225 km depth for the laterally varying viscosity case (Figure 11a). By comparison, of the 895 continental splitting measurements, 33% of stations are fit to within 25° and 61% of stations are fit better than 45° (Figure 11b). Because there are so many continental stations, we can be more than 99% confident that this distribution of continental misfits (Figure 11b) does not occur randomly [*Press et al.*, 1992, pp. 609–615]. (Although there are nearly 50 times fewer oceanic stations, the small misfits for these stations allows us to be equally confident that the oceanic distribution is not random.) Thus our "preferred" model slightly improves the fit for continental stations compared to a random distribution. This hints that asthenospheric anisotropy may contribute regionally to the net anisotropy in some continental areas.

[36] The average fit for the layered viscosity case is comparable to that of the laterally varying case (Figure 11b), although regionally the average misfit may be significantly improved (South America, Figure 11d) or degraded (Eurasia, Figure 11e) by the introduction of laterally varying viscosity. This shows that asthenospheric anistropy is sensitive to the viscosity structure of the continental lithosphere, and leaves open the possibility that refinement of the asthenospheric flow model beneath continents could improve the prediction of continental splitting observations. On the other hand, the fact that lateral viscosity variations do not significantly improve the global average fit to continental anisotropy (Figure 11b) suggests that LPO development in the asthenosphere flow is not the primary source of continental anisotropy. Rather, splitting observations made on continents may be dominated by fossil lithospheric fabric, which cannot be predicted by mantle flow models.

5. Discussion

[37] The observation that $\Pi < 0.5$ throughout most of the asthenosphere implies that the ISA can be used as an

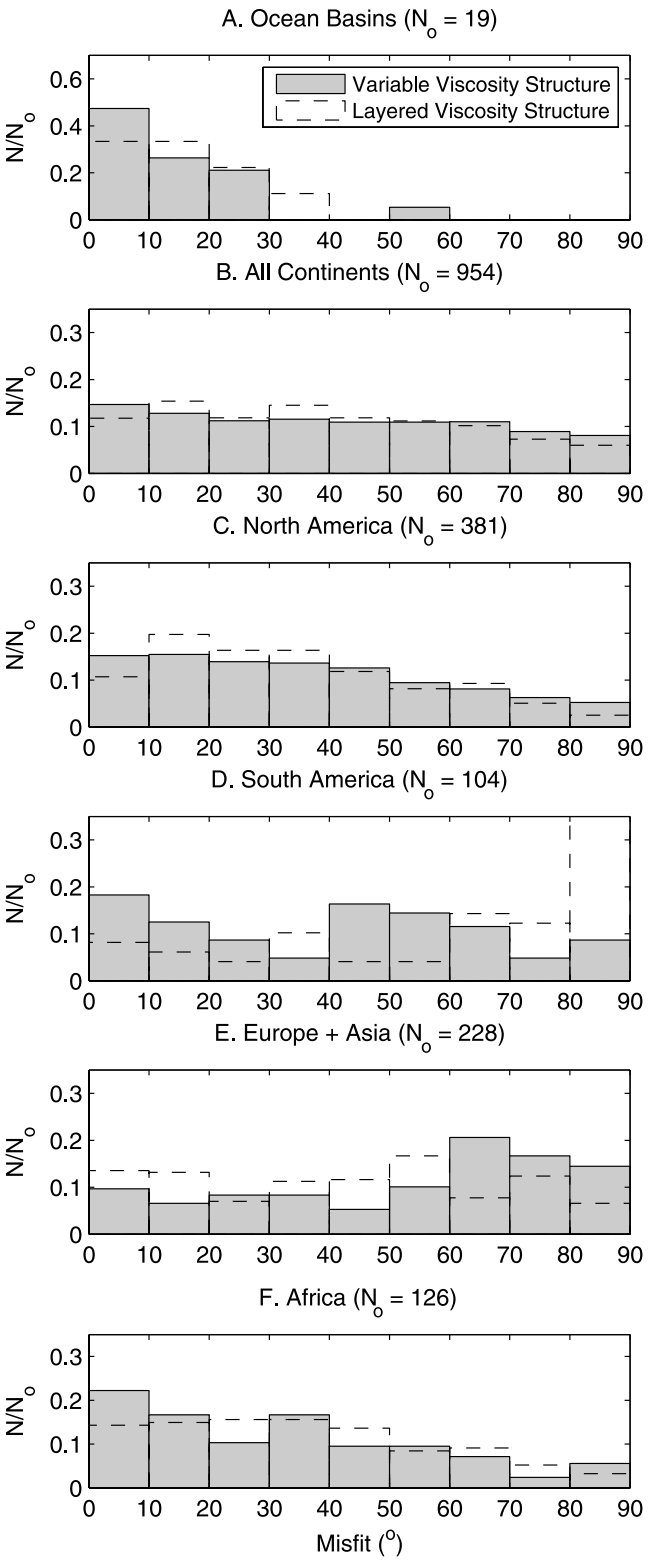

Figure 11. Histogram showing the misfit (in 10° depth bins) for (a) oceanic, (b) continental, (c) North American, (d) South American, (e) Eurasian, and (f) African stations between SKS observations and predictions of ISA at 225 km for the layered (dashed boundaries) and laterally varying (gray, solid boundaries) viscosity structures. We combine plate-driven and density-driven flows using a value of β = 0.5 consistent with the "preferred" model in both cases.

approximation for LPO in most locations [*Kaminski and Ribe*, 2002]. This greatly simplifies the prediction of asthenospheric anisotropy because the full determination of LPO is computationally expensive and complicated [*Kaminski et al.*, 2004], and requires an accurate method to trace finite strain accumulation along flow lines [e.g., *Becker et al.*, 2003]. Such a method cannot be implemented from "instantaneous" flow models that predict the present-day flow field because such models do not take into account the time dependence of mantle flow. Furthermore, uncertainty in the rates of grain boundary migration and dynamic recrystallization may introduce uncertainty into the calculation of LPO [*Kaminski and Ribe*, 2001]. By contrast, the ISA can be determined from an instantaneous "snapshot" of the mantle flow field without considering the time-dependent accumulation of finite strain. The few areas of the asthenosphere where long-wavelength upwellings (African Superplume, Figure 5d) or downwellings (Farallon slab, Figure 5c) rotate LPO away from the ISA can easily be identified using the $\Pi < 0.5$ cutoff criterion. This criterion is also useful for differentiating regions with significant anisotropy-producing shear flow (low Π) from the slowly deforming lithospheric regions (large Π) where anisotropy may be associated with past deformation (Figures 4 and 5).

[38] Short-wavelength complexities to the flow field are more problematic because our global flow model (with 157 km horizontal resolution) cannot resolve details of flow associated with plate boundaries, localized convective downwelling, or upwelling plumes. Thus we may predict $\Pi < 0.5$ even though more detailed models might predict $\Pi > 0.5$. Because this is likely true at certain plate boundaries, we have ignored stations near plate boundaries when constraining our model using observed splitting data. It is not known, however, which parts of the lithosphere might be currently experiencing localized convective downwelling because such downwellings likely remove only the lower part of the lithospheric layer and are difficult to detect from the surface [*Conrad and Molnar*, 1997]. If downwelling instability is present beneath a station, flow from this downwelling will influence LPO in an unpredictable way, and could generate LPO that is unrelated to background mantle flow. However, localized convective downwelling is likely to be short-lived and infrequent in most environments [e.g., *Conrad and Molnar*, 1999], and thus unlikely to affect large numbers of shear wave splitting measurements. The fact that we fit the oceanic shear wave splitting data to $\sim$13° indicates that anisotropy beneath most oceanic stations is not strongly influenced by localized convective downwelling. Similarly, although localized upwelling from mantle plumes may influence many of the oceanic island stations used for our inversion, our successful prediction of oceanic anisotropy suggests that these local upwellings do not strongly perturb shear wave splitting measurements at these oceanic stations. Furthermore, *Kaminski and Ribe* [2002] showed that the ISA direction does not differ significantly from the background shear direction directly above an upwelling plume. Thus, while we have ignored convective instability and upwelling plumes in our analysis of oceanic anisotropy, their influence is probably not significant for oceanic stations.

[39] The ISA calculated from global mantle flow models does a good job of explaining observed shear wave splitting

measurements in oceanic regions. Our results confirm those of *Behn et al.* [2004], who showed that both plate-driven and mantle-driven flows are necessary to explain splitting observations at oceanic stations surrounding Africa. We find that an asthenospheric viscosity of $\sim 5 \times 10^{19}$ Pa s generates rates of asthenospheric flow driven by mantle density heterogeneity that, when combined with shear flow associated with plate motions, best explains oceanic anisotropy. This result is nearly identical to that obtained by *Behn et al.* [2004], despite the fact that *Behn et al.* [2004] used a spectral code that could not handle lateral viscosity variations and used the direction of maximum shear, rather than the ISA, to predict anisotropy (the fact that horizontal shear nearly parallels the ISA explains why studies that use the former as an approximation for LPO [e.g., *Gaboret et al.*, 2003; *Behn et al.*, 2004] do an excellent job of predicting oceanic anisotropy). Most of the stations that we have added to the *Behn et al.* [2004] analysis are on the fast moving Pacific or Australian plates, where plate-driven flow dominates observed anisotropy. Thus additional shear wave splitting measurements made on slowly moving plates in the Atlantic or Indian basins are crucial to further constraining the relative importance of plate-driven and density-driven asthenospheric flows. Oceanic anisotropy inferred from surface wave models [e.g., *Becker et al.*, 2003; *Debayle et al.*, 2005] should also provide useful constraints because coverage is more globally uniform (although less horizontally resolved) than shear wave splitting observations.

[40] The fact that our flow models predict oceanic anisotropy significantly better than continental anisotropy can be explained in several ways. First, while our models seem to accurately predict flow beneath oceanic lithosphere, they may do so more poorly beneath continents. This would be the case if the viscosity and/or density structures beneath continents are not accurately characterized due to poor constraints on these parameters. Alternatively, it is possible that our shear flow approximation is less appropriate for subcontinental asthenosphere than it is for oceans. Although horizontal velocity gradients, which are not included in our analysis, might be enhanced by lithospheric thickness variations (Figure 3), their effect should be offset by larger vertical velocity gradients caused by narrowing of the asthenospheric channel beneath thicker lithosphere. Future calculations with greater horizontal resolution may be able to address these effects. A poorer fit to the continental splitting data could also result if small-scale convection is more prevalent beneath continents (as we might expect because continental interiors are typically thicker and more actively deforming than oceanic lithosphere away from plate boundaries [e.g., *Conrad*, 2000]), or if subcontinental shear flow produces a different anisotropic fabric than does shear flow beneath oceans (where A-type fabric successfully predicts anisotropy). However, non-A-type fabrics are expected primarily at high water contents [*Jung and Karato*, 2001], and the presence of water is probably only a factor near plate boundaries and not preferentially beneath continents. Thus we cannot rule out the possibility that continental anisotropy may be dominated by an asthenospheric component that is not correctly predicted by our current models.

[41] Another, perhaps more likely, explanation for why asthenospheric shear flow successfully predicts anisotropy in oceanic areas but fails to do so for continents is the possibility that lithospheric anisotropy, which cannot be predicted by our models, is more significant for continents than it is for oceans. In fact, lithospheric anisotropy has been invoked to explain anisotropy in several continental regions. First, lithospheric deformation associated with orogenic deformation may induce significant anisotropy into the lithospheric fabric [*Silver*, 1996]. This may explain, for example, our poor prediction of asthenospheric anisotropy (Figure 8) in the Alpine and Tibetan orogenic zones. Second, because cratonic lithosphere is old, thick, and cold, lithospheric anisotropy created by any past deformation may be preserved for long periods of geologic time. For example, *Silver and Chan* [1988] and *Silver et al.* [2004, 2006] argue that patterns of anisotropy observed in southern Africa (Figure 8) are associated with Precambrian lithospheric deformation. Although the generally NE-SW orientation of anisotropy in southern Africa is consistent with an asthenospheric contribution (Figures 8 and 11f), local deviations over short spatial scales argues for a strong lithospheric component in these data [*Fouch et al.*, 2004]. Furthermore, other cratonic areas (Canadian, Siberian) are poorly fit by asthenospheric shear flow (Figure 8). Thus the presence of lithospheric anisotropy in many continental areas may explain why our predictions of asthenospheric anisotropy fit the continental splitting data more poorly than they do the oceanic data.

[42] Despite the likely presence of an anisotropic continental lithosphere, the fit to continental anisotropy is improved in some areas by the introduction of lateral variations in lithospheric viscosity (Figure 11), suggesting an asthenospheric component to some continental anisotropy. For example, the introduction of lateral viscosity variations improves the average fit for North American splitting observations (Figure 11c), particularly in areas away from cratons (eastern and western North America, Figure 8). Lateral viscosity variations also improve the fit for Africa (Figure 11f) and South America (Figure 11d), although the station coverage for these continents is poor (Figure 8) and overlaps areas where we expect significant lithospheric anisotropy (e.g., southern Africa). On the other hand, the introduction of lateral viscosity variations in Eurasia degrades the fit to observed anisotropy (Figure 11e). This may indicate problems with the Eurasian lithospheric thickness model (Figure 3a), although many European and Asian data are located in orogenic or cratonic areas where we expect significant lithospheric anisotropy (Figure 8). Alternatively, the oceanic flow model may not be appropriate for this very large, slowly moving continental area. Clearly a more detailed study of individual continental regions [e.g., *Fouch and Rondenay*, 2006] is required to assess regional variations in the relative importance of lithospheric and asthenospheric contributions to continental anisotropy.

[43] There are several reasons why we might expect continental lithosphere to be more anisotropic than oceanic lithosphere. First, because continental lithosphere is older and colder than oceanic lithosphere [e.g., *Rudnick et al.*, 1998], it may better preserve tectonic fabric imparted to it due to previous deformation over geologic time [e.g., *Savage*, 1999]. Continental lithosphere also experiences more deformation than does oceanic lithosphere due to the fact that it participates in continent-continent collisions

which may occur multiple times over the greater lifetime of continents. Furthermore, greater continental lithosphere thickness provides a thicker layer for preserving lithospheric anisotropy. Finally, dislocation creep rheology, which generates anisotropic LPO, is only dominant over diffusion creep down to 250–350 km depth [e.g., *Hirth and Kohlstedt*, 2003]. Thick continental roots may push the sublithospheric deforming region below this depth, thus preventing the development of anisotropic fabric by asthenospheric flow.

[44] The spatial distribution of shear wave splitting observations is highly variable (Figure 8). Oceanic coverage is particularly sparse, and continental coverage includes some areas with excellent (North America, Europe, and southern Africa) and some with very poor (Australia, Amazonia, Antarctica, the rest of Africa) spatial coverage. Thus a complete characterization of continental anisotropy (lithospheric and asthenospheric components) requires significantly better spatial coverage of shear wave splitting observations. Surface wave anisotropy models [e.g., *Becker et al.*, 2003; *Nettles and Dziewónski*, 2004; *Debayle et al.*, 2005] could be especially useful because they provide some depth resolution that could be used to separate the lithospheric and asthenospheric components of the net anisotropy measured by shear wave splitting. Initial analyses of surface wave studies do suggest differences between continental and oceanic anisotropy with patterns consistent with the model predictions made here. For example, the azimuthal anisotropy model of *Debayle et al.* [2005] shows a slightly deeper peak in the magnitude of anisotropy ($\sim$100 km) for oceans than for continents ($\sim$50 km). This suggests a shallow lithospheric source of anisotropy dominates for continents, and a deeper asthenospheric origin for oceans. Similar patterns are seen in regional studies of North America, where the strongest azimuthal anisotropy is found between 100 and 200 km beneath the eastern Pacific Ocean and the Basin and Range province but at shallower depths (50–100 km) beneath the North American craton [*Nettles and Dziewónski*, 2004]. The presence of significant anisotropy beneath the Basin and Range is consistent with our predictions for western North America (Figure 8) and with other anisotropy studies [*Silver and Holt*, 2002; *Becker et al.*, 2006b], which suggests that asthenospheric flow may contribute to continental anisotropy in some areas.

6. Conclusions

[45] We have shown that viscous deformation in the asthenosphere tends to align the LPO of olivine aggregates with the infinite strain axis (ISA) corresponding to their orientation after infinite deformation. This is because asthenospheric shear flow rotates the LPO of olivine aggregates toward the ISA faster than the complexities of the flow can change the sense of deformation that these olivine aggregates experience. *Kaminski and Ribe* [2002] expressed this comparison of rates within their definition of the grain orientation lag parameter Π, which we have shown is small throughout the asthenosphere away from plate boundaries. This means that the strain history of flow need only be considered in a few locations (such as plate boundaries) where the flow field is extremely time-dependent or changes rapidly along flow lines. This is an important simplification because computing strain deformation is expensive and may involve complicated (and often poorly constrained) modeling of the time dependence of the flow field [e.g., *Becker et al.*, 2003]. This is particularly true if the effects of dynamic recrystallization [*Kaminski and Ribe*, 2001; *Kaminski et al.*, 2004] are taken into account along with finite strain [*Becker et al.*, 2006a]. By contrast, the ISA and Π can be calculated easily from any given flow field and its time derivative.

[46] Using the assumption that the ISA orientation approximates asthenospheric LPO, we have shown that shear wave splitting observations in oceanic regions are well fit by asthenospheric shear flow driven by a combination of plate motions and mantle density heterogeneity inferred from seismic tomography [e.g., *Behn et al.*, 2004]. Furthermore, the fact that $\Pi < 0.5$ throughout most of the asthenosphere implies that the direction of asthenospheric anisotropy beneath the ocean basins is a reasonable approximation for the direction of asthenospheric flow in most locations away from plate boundaries [*Kaminski and Ribe*, 2002]. By contrast, continental anisotropy is more poorly fit than the oceanic data by the ISA. However, the average fit to continental shear wave splitting measurements is improved compared to a random distribution, suggesting that sublithospheric viscous flow in the asthenosphere may also contribute to splitting observations in some continental areas.

[47] We conclude that viscous shear flow in the asthenosphere controls LPO formation and produces an asthenospheric layer of flow-induced anisotropy worldwide. In oceanic regions, which feature a thin lithosphere with little history of tectonic deformation, this asthenospheric anisotropy largely explains shear wave splitting measurements made at oceanic stations. Asthenospheric anisotropy is probably present beneath continents as well; however, in these regions the lithosphere may retain a fossil fabric that controls the net anisotropy. Our conclusion that asthenospheric anisotropy dominates beneath oceans, but lithospheric anisotropy may dominate in continental areas is consistent with surface wave tomography studies [e.g., *Nettles and Dziewónski*, 2004; *Debayle et al.*, 2005]. This conclusion is consistent with the thicker, older, and more deformed nature of continental lithosphere. Given that all of these factors promote the development of an anisotropic lithosphere, it is not surprising that oceanic anisotropy can be largely explained by asthenospheric flow while a fossil lithosphere fabric must be invoked to explain continental anisotropy.

[48] **Acknowledgments.** We thank Neil Ribe and an anonymous referee for reviews that helped improve the manuscript, and NSF grants EAR-0509882 (M.D.B. and C.P.C.), EAR-0609590 (C.P.C.), and EAR-0215616 (P.G.S.) for financial support.

References

Assumpcão, M., M. Heintz, A. Vauchez, and M. E. Silva (2006), Upper mantle anisotropy in SE and central Brazil from SKS splitting: Evidence of asthenospheric flow around a cratonic keel, *Earth Planet. Sci. Lett.*, *250*, 224–240.

Becker, T. W. (2006), On the effect of temperature and strain-rate dependent viscosity on global mantle flow, net rotation, and driving forces, *Geophys. J. Int.*, *167*, 943–957.

Becker, T. W., J. B. Kellogg, G. Ekstrom, and R. J. O'Connell (2003), Comparison of azimuthal seismic anisotropy from surface waves and finite strain from global mantle-circulation models, *Geophys. J. Int.*, *155*, 696–714.

Becker, T. W., S. Chevrot, V. Schulte-Pelkum, and D. K. Blackman (2006a), Statistical properties of seismic anisotropy predicted by upper mantle geodynamic models, *J. Geophys. Res.*, *111*, B08309, doi:10.1029/2005JB004095.

Becker, T. W., V. Schulte-Pelkum, D. K. Blackman, J. B. Kellogg, and R. J. O'Connell (2006b), Mantle flow under the western United States from shear wave splitting, *Earth Planet. Sci. Lett.*, *247*, 235–251.

Behn, M. D., C. P. Conrad, and P. G. Silver (2004), Detection of upper mantle flow associated with the African Superplume, *Earth Planet. Sci. Lett.*, *224*, 259–274.

Blackman, D. K., H.-R. Wenk, and J. M. Kendall (2002), Seismic anisotropy in the upper mantle: 1. Factors that affect mineral texture and effective elastic properties, *Geochem. Geophys. Geosyst.*, *3*(9), 8601, doi:10.1029/2001GC000248.

Çadek, O., and L. Fleitout (2003), Effect of lateral viscosity variations in the top 300 km on the geoid and dynamic topography, *Geophys. J. Int.*, *152*, 566–580.

Conrad, C. P. (2000), Convective instability of thickening mantle lithosphere, *Geophys. J. Int.*, *143*, 52–70.

Conrad, C. P., and M. Gurnis (2003), Seismic tomography, surface uplift, and the breakup of Gondwanaland: Integrating mantle convection backwards in time, *Geochem. Geophys. Geosyst.*, *4*(3), 1031, doi:10.1029/2001GC000299.

Conrad, C. P., and C. Lithgow-Bertelloni (2006), Influence of continental roots and asthenosphere on plate-mantle coupling, *Geophys. Res. Lett.*, *33*, L05312, doi:10.1029/2005GL025621.

Conrad, C. P., and P. Molnar (1997), The growth of Rayleigh-Taylor-type instabilities in the lithosphere for various rheological and density structures, *Geophys. J. Int.*, *129*, 95–112.

Conrad, C. P., and P. Molnar (1999), Convective instability of a boundary layer with temperature- and strain-rate-dependent viscosity in terms of "available buoyancy," *Geophys. J. Int.*, *139*, 51–68.

Cordier, P., T. Ungár, L. Zsoldos, and G. Tichy (2004), Dislocation creep in $MgSiO_3$ perovskite at conditions of the Earth's uppermost lower mantle, *Nature*, *428*, 837–840.

Debayle, E., B. Kennett, and K. Priestley (2005), Global azimuthal seismic anisotropy and the unique plate-motion deformation of Australia, *Nature*, *433*, 509–512.

DeMets, C., R. G. Gordon, D. F. Argus, and S. Stein (1994), Effect of recent revisions to the geomagnetic reversal time scale on estimates of current plate motions, *Geophys. Res. Lett.*, *21*, 2191–2194.

Engebretson, D. C., A. Cox, and R. G. Gordon (1984), Relative motions between oceanic plates of the Pacific basin, *J. Geophys. Res.*, *89*, 10,291–10,310.

Fontaine, F. R., E. E. E. Hooft, P. G. Burkett, D. R. Toomey, S. C. Solomon, and P. G. Silver (2005), Shear-wave splitting beneath the Galápagos archipelago, *Geophys. Res. Lett.*, *32*, L21308, doi:10.1029/2005GL024014.

Forsyth, D. W. (1975), The early structural evolution and anisotropy of the oceanic upper mantle, *Geophys. J. R. Astron. Soc.*, *43*, 103–162.

Fouch, M. J., and S. Rondenay (2006), Seismic anisotropy beneath stable continental interiors, *Phys. Earth Planet. Inter.*, *158*, 292–320.

Fouch, M. J., K. M. Fischer, M. E. Wysession, and T. J. Clarke (2000), Shear wave splitting, continental keels, and patterns of mantle flow, *J. Geophys. Res.*, *105*, 6255–6276.

Fouch, M. J., P. G. Silver, D. R. Bell, and J. N. Lee (2004), Small-scale variations in seismic anisotropy near Kimberley, South Africa, *Geophys. J. Int.*, *157*, 764–774.

Gaboret, C., A. M. Forte, and J.-P. Montagner (2003), The unique dynamics of the Pacific hemisphere mantle and its signature on seismic anisotropy, *Earth Planet. Sci. Lett.*, *208*, 219–233.

Gung, Y., M. Panning, and B. Romanowicz (2003), Global anisotropy and the thickness of continents, *Nature*, *422*, 707–711, doi:10.1038/nature01559.

Hager, B. H., and R. J. O'Connell (1981), A simple global model of plate dynamics and mantle convection, *J. Geophys. Res.*, *86*, 4843–4867.

Hammond, J. O. S., J.-M. Kendall, G. Rümpker, J. Wookey, N. Teanby, P. Joseph, T. Ryberg, and G. Stuart (2005), Upper mantle anisotropy beneath the Seychelles microcontinent, *J. Geophys. Res.*, *110*, B11401, doi:10.1029/2005JB003757.

Hess, H. H. (1964), Seismic anisotropy of the uppermost mantle under oceans, *Nature*, *203*, 629–631.

Hirth, G., and D. L. Kohlstedt (1996), Water in the oceanic upper mantle: Implications for rheology, melt extraction and the evolution of the lithosphere, *Earth Planet. Sci. Lett.*, *144*, 93–108.

Hirth, G., and D. L. Kohlstedt (2003), Rheology of the upper mantle and the mantle wedge: A view from the experimentalists, in *Inside the Subduction Factory*, *Geophys. Monogr. Ser.*, vol. 138, edited by J. Eiler, pp. 83–105, AGU, Washington, D. C.

Holtzman, B. K., D. L. Kohlstedt, M. E. Zimmerman, F. Heidelbach, T. Hiraga, and J. Hustoft (2003), Melt segregation and strain partitioning: Implications for seismic anisotropy and mantle flow, *Science*, *301*, 1227–1230.

Ismail, W. B., and D. Mainprice (1998), An olivine fabric database: An overview of upper mantle fabrics and seismic anisotropy, *Tectonophysics*, *296*, 145–157.

Jordan, T. H. (1975), The continental tectosphere, *Rev. Geophys.*, *13*, 1–12.

Jung, H., and S.-I. Karato (2001), Water-induced fabric transitions in olivine, *Science*, *293*, 1460–1463.

Kaminski, E., and N. M. Ribe (2001), A kinematic model for the recrystallization and texture development in olivine polycrystals, *Earth Planet. Sci. Lett.*, *189*, 253–267.

Kaminski, E., and N. M. Ribe (2002), Timescales for the evolution of seismic anisotropy in mantle flow, *Geochem. Geophys. Geosyst.*, *3*(8), 1051, doi:10.1029/2001GC000222.

Kaminski, E., N. M. Ribe, and J. T. Browaeys (2004), D-rex, a program for calculation of seismic anisotropy due to crystal lattice preferred orientation in the convective upper mantle, *Geophys. J. Int.*, *158*, 744–752.

Karato, S.-I., and B. B. Karki (2001), Origin of lateral variation of seismic wave velocities and density in the deep mantle, *J. Geophys. Res.*, *106*, 21,771–21,783.

Karato, S.-I., and P. Wu (1993), Rheology of the upper mantle: A synthesis, *Science*, *260*, 771–778.

Katayama, I., H. Jung, and S.-I. Karato (2004), New type of olivine fabric from deformation experiments at modest water content and low stress, *Geology*, *32*, 1045–1048.

Klosko, E. R., R. M. Russo, E. A. Okal, and W. P. Richardson (2001), Evidence for a rheologically strong chemical mantle root beneath the Ontong-Java Plateau, *Earth Planet. Sci. Lett.*, *186*, 347–361.

Kneller, E. A., P. E. van Keken, S.-I. Karato, and J. Park (2005), B-type olivine fabric in the mantle wedge: Insights from high-resolution non-Newtonian subduction zone models, *Earth Planet. Sci. Lett.*, *237*, 781–797.

Lithgow-Bertelloni, C., and P. G. Silver (1998), Dynamic topography, plate driving forces and the Africa superswell, *Nature*, *395*, 269–272.

Malvern, L. E. (1969), *Introduction to the Mechanics of a Continuous Medium*, Prentice-Hall, Englewood Cliffs, N. J.

McKenzie, D. (1979), Finite deformation during fluid flow, *Geophys. J. R. Astron. Soc.*, *58*, 689–715.

Meade, C., P. G. Silver, and S. Kaneshima (1995), Laboratory and seismological observations of lower mantle isotropy, *Geophys. Res. Lett.*, *22*, 1293–1296.

Mitrovica, J. X. (1996), Haskell [1935] revisited, *J. Geophys. Res.*, *101*, 555–569.

Montagner, J.-P. (1994), Can seismology tell us anything about convection in the mantle?, *Rev. Geophys.*, *32*, 115–138.

Moresi, L., S. Zhong, and M. Gurnis (1996), The accuracy of finite element solutions of Stokes flow with strongly varying viscosity, *Phys. Earth Planet. Inter.*, *97*, 83–94.

Müller, R. D., W. R. Roest, J.-Y. Royer, L. M. Gahagan, and J. G. Sclater (1997), Digital isochrons of the world's ocean floor, *J. Geophys. Res.*, *102*, 3211–3214.

Nettles, M., and A. M. Dziewónski (2004), Integrating global and regional datasets for tomography in North America, *Eos Trans. AGU*, *85*(47), Fall Meet. Suppl., Abstract S52-04.

Park, J., and V. Levin (2002), Seismic anisotropy: Tracing plate dynamics in the mantle, *Science*, *296*, 485–489.

Peyton, V., V. Levin, J. Park, M. Brandon, J. Lees, E. Gordeev, and A. Ozerov (2001), Mantle flow at a slab edge: Seismic anisotropy in the Kamchatka region, *Geophys. Res. Lett.*, *28*, 379–382.

Press, W. H., B. P. Flannery, S. A. Teukolsky, and W. T. Vetterling (1992), *Numerical Recipes in FORTRAN*, Cambridge Univ. Press, New York.

Ribe, N. M. (1989), Seismic anisotropy and mantle flow, *J. Geophys. Res.*, *94*, 4213–4223.

Ribe, N. M. (1992), On the relation between seismic anisotropy and finite strain, *J. Geophys. Res.*, *97*, 8737–8747.

Ritsema, J., H. J. van Heijst, and J. H. Woodhouse (2004), Global transition zone tomography, *J. Geophys. Res.*, *109*, B02302, doi:10.1029/2003JB002610.

Rudnick, R., W. McDonough, and R. J. O'Connell (1998), Thermal structure, and composition of the continental lithosphere, *Chem. Geol.*, *145*, 295–411.

Rumpker, G., and P. G. Silver (1998), Apparent shear-wave splitting parameters in the presence of vertically-varying anisotropy, *Geophys. J. Int.*, *135*, 790–800.

Russo, R. M., and P. G. Silver (1994), Trench-parallel flow beneath the Nazca plate from seismic anisotropy, *Science*, *263*, 1105–1111.

Savage, M. K. (1999), Seismic anisotropy and mantle deformation: What have we learned from shear wave splitting?, *Rev. Geophys.*, *37*, 65–106.

Sella, G. F., T. H. Dixon, and A. Mao (2002), REVEL: A model for recent plate velocities from space geodesy, *J. Geophys. Res.*, *107*(B4), 2081, doi:10.1029/2000JB000033.

Silver, P. G. (1996), Seismic anisotropy beneath the continents: Probing the depths of geology, *Annu. Rev. Earth Planet. Sci.*, *24*, 385–432.
Silver, P. G., and W. W. Chan (1988), Implications for continental structure and evolution from seismic anisotropy, *Nature*, *335*, 34–39.
Silver, P. G., and W. E. Holt (2002), The mantle flow field beneath western North America, *Science*, *295*, 1054–1057.
Silver, P. G., and M. K. Savage (1994), The interpretation of shear-wave splitting parameters in the presence of two anisotropic layers, *Geophys. J. Int.*, *119*, 949–963.
Silver, P. G., S. S. Gao, K. H. Liu, and The Kaapval Seismic Group (2001), Mantle deformation beneath southern Africa, *Geophys. Res. Lett.*, *28*, 2493–2496.
Silver, P. G., M. J. Fouch, S. S. Gao, and M. Schmitz (2004), Seismic anisotropy, mantle fabric, and the magmatic evolution of Precambrian southern Africa, *S. Afr. J. Geol.*, *107*, 45–58.
Silver, P. G., M. Behn, K. Kelley, M. Schmitz, and B. Savage (2006), Understanding cratonic flood basalts, *Earth Planet. Sci. Lett.*, *245*, 190–201.
Smith, G. P., D. A. Wiens, K. M. Fischer, L. M. Dorman, S. C. Webb, and J. A. Hildebrand (2001), A complex pattern of mantle flow in the Lau backarc, *Science*, *292*, 713–716.
Stein, C. A., and S. Stein (1992), A model for the global variation in oceanic depth and heat flow with lithospheric age, *Nature*, *359*, 123–129.
Turcotte, D. L., and E. R. Oxburgh (1967), Finite amplitude convective cells and continental drift, *J. Fluid Mech.*, *28*, 29–42.
Verma, R. K. (1960), Elasticity of some high-density crystals, *J. Geophys. Res.*, *65*, 757–766.
Walker, K. T., G. H. R. Bokelmann, S. L. Klemperer, and A. Nyblade (2005), Shear-wave splitting around hotspots: Evidence for upwelling-related mantle flow?, *Spec. Pap. Geol. Soc. Am.*, *388*, 171–192.
Wen, L., and D. L. Anderson (1997), Present-day plate motion constraint on mantle rheology and convection, *J. Geophys. Res.*, *102*, 24,639–24,653.
Wolfe, C. J., and P. G. Silver (1998), Seismic anisotropy of oceanic upper mantle: Shear wave splitting methodologies and observations, *J. Geophys. Res.*, *103*, 749–771.
Wolfe, C. J., and S. C. Solomon (1998), Shear-wave splitting and implications for mantle flow beneath the MELT region of the East Pacific Rise, *Science*, *280*, 1230–1232.
Xue, M., and R. M. Allen (2005), Asthenospheric channeling of the Icelandic upwelling: Evidence from seismic anisotropy, *Earth Planet. Sci. Lett.*, *235*, 167–182.
Zhang, S., and U. Christensen (1993), Some effects of viscosity variations on geoid and surface velocities induced by density anomalies in the mantle, *Geophys. J. Int.*, *114*, 531–547.
Zhang, S., and S.-I. Karato (1995), Lattice preferred orientation of olivine aggregates deformed in simple shear, *Nature*, *375*, 774–777.
Zhong, S. (2001), Role of ocean-continent contrast and continental keels on plate motion, net rotation of the lithosphere, and the geoid, *J. Geophys. Res.*, *106*, 703–712.
Zhong, S., M. T. Zuber, L. N. Moresi, and M. Gurnis (2000), The role of temperature-dependent viscosity and surface plates in spherical shell models of mantle convection, *J. Geophys. Res.*, *105*, 11,063–11,082.

M. D. Behn, Department of Geology and Geophysics, Woods Hole Oceanographic Institution, Woods Hole, MA 02543, USA.
C. P. Conrad, Department of Earth and Planetary Sciences, Johns Hopkins University, 301 Olin Hall, 3400 Charles Street, Baltimore, MD 21218, USA. (conrad@jhu.edu)
P. G. Silver, Department of Terrestrial Magnetism, Carnegie Institution of Washington, Washington, DC 20015, USA.